Bulletin of Earthquake Engineering (2023) 21:1017–1045
https://doi.org/10.1007/s10518-022-01565-y

ORIGINAL ARTICLE

Damage control of the masonry infills in RC frames under cyclic loads: a full-scale test study and numerical analyses

Qiwang Su[1] · Gaochuang Cai[2,3] · Meree Hani[4] · Amir Si Larbi[2,3] · Konstantinos Daniel Tsavdaridis[2,5]

Received: 3 February 2022 / Accepted: 1 November 2022 / Published online: 27 November 2022

Abstract
This study investigates the effect of damage control methods on the seismic performance of masonry infilled walls in reinforced concrete (RC) frames, by experimentally investigating three full-scale infilled RC frames with different treatment details and finite element method (FEM) analysis. The control methods included full-length connecting steel rebars, styrene butadiene styrene (SBS) sliding layers, and two gaps between the wall and frame columns. The results indicated that the ductility, wall damage, and residual deformation of the frame with gaps or SBS layers were significantly improved. However, the initial stiffness, energy dissipation capacity, and lateral load-carrying capacity of the frames with SBS sliding layers all were reduced. The fully infilled frames exhibited a better lateral load-carrying capacity, stiffness, and energy dissipation capacity, but presented larger lateral residual deformation and lower ductility. The damage of the infilled walls in RC frames can be controlled by using longer connecting rebars. The gaps and sliding layers can both significantly reduce the in-plane damage of the walls. A simplified FEM model was proposed and applied to conduct a parametric analysis for an in-depth study of fully infilled RC frames with and without sliding layers. The results show that SBS is the optimal sliding layer material, and its optimal spacing in RC frames is recommended as 1000 mm.

Keywords Damage control · Masonry hollow bricks · Sliding layers · Wall collapse ratio · FEM

✉ Gaochuang Cai
gaochuang.cai@enise.fr

1 School of Civil Engineering, Southwest Jiaotong University, Chengdu, Sichuan, China

2 International Research Organization for Advanced Science and Technology (IROAST), Kumamoto University, Kumamoto, Japan

3 Université de Lyon, Ecole Centrale de Lyon – ENISE, LTDS, CNRS UMR 5513, 58 Rue Jean Parot, 42000 Saint-Etienne, France

4 State Key Laboratory of Geohazard Prevention and Geoenvironment Protection, Chengdu University of Technology, Chengdu, Sichuan, China

5 Department of Engineering, School of Science & Technology, City, University of London, Northampton Square, London EC1V 0HB, UK

List of symbols

A_{cp}	Collapsed and crushed area of infilled walls
A_p	Total area of the infilledwall of RC frames
b	Width of section
b_f	Width of flange
F	Lateral load
h	Total thickness of section
h_f	Total thickness of the flange
K	Unloading stiffness
K_{int}	Initial stiffness
K_y	Yielding stiffness
R_{res}	Lateral residual deformation
V_{max}	Maximum lateral load
W	Maximum strain energy of a given cycle
CC	Corner crushing mode
SS	Sliding shear mode
DC	Diagonal compression mode
DK	Diagonal cracking mode
FF	Frame failure mode
Δ_y	Yielding displacement
Δ_{max}	Maximum displacement
Δ_u	Ultimate displacement
μ_{max}	Maximum ductility
μ_u	Ultimate ductility
δ	Lateral deformation
δ_u	Inter-story drift ratio
δ_R	Residual deformation
υ_{eq}	Fraction of critical damping
ΔW	Energy loss per cycle in sinusoidal vibration
γ	Wall collapse ratio

1 Introduction

Most of the infill in existing reinforced concrete (RC) frame structures in the world are still made of unreinforced brick/block masonry. There is usually an interaction between non-structural infill panels and the primary structural frame elements under an earthquake. The influence of infills may positively or negatively affect the seismic vulnerability of the RC frames, depending on the properties of masonry and the regularity of their disposition (Uva et al. 2012; Bartolomeo Pantò et al. 2017). In China the load-carrying of infilled walls is usually ignored in the design of RC frame structures for they are used just to divide the space, however, their weight is added to the frames as a fixed force. In this case, more and more lightweight infilled walls are used in filled RC frames, such as masonry hollow brick (MHB). On the other hand, MHBs can minimize the adverse impact of the infilled walls on their surrounding frame beams and columns. However, the walls are easy to be damaged under reversed lateral loads caused by earthquakes for their low strength and large void ratio, which seriously affects the use of residents and causes huge economic and social losses. This fact means that infill wall damage during earthquakes needs to be controlled (Proença2012; Costa et al. 2014; Goncalves2018).

Up to now, many treatment methods have been proposed for controlling the damage of infilled walls under earthquakes. They can be mainly divided into two types, (1) strengthening or improving structural materials such as using shock-absorbing mortars and steel fiber mortars, and (2) structural measures for infills such as reinforcing the infills (Soti2014; Triwiyono2015), adding damping or energy dissipation devices, and separating infills from the frame beams and columns (Zhou Yun et al. 2013). Wang and Ye (Wang 2015; Yanhua et al. 2004) suggested using rubber concrete and foamed concrete blocks to improve the seismic behavior of RC frames respectively and studied their seismic performance experimentally and numerically. Moghadam et al. (2006) proposed to use RC panels to reinforce infilled walls in RC frames and studied their horizontal reinforcement and bond beams effect through experiments. Sahota and Riddington (2001) proposed to install a lead layer between infilled wall and frame beams based on the theory of frame column creep shortening. Mohammadi and Akramir (2005) analyzed the seismic performance of RC frames after removing their infilled wall corners and partially weakening RC frame columns. Their results showed the developed system acted as a sacrificial element just like a fuse to protect the infilled walls and frame elements. Yang and Ou et al. (2011) commented that the damage of the infill wall frames with energy dissipating devices wall was reduced. Zhou et al. (2014) reported that the seismic performance of RC frames with viscous dampers and styrene-butadiene-styrene thermoplastic elastomer (SBS) and the damage control of their walls were improved significantly. Perera et al. (2004) proposed an infill panel with K-bracing containing a vertical shear link. With this approach, the stiffening effect provided by the masonry was kept while the low ductility of the frames was compensated with the energy dissipation action of used link elements.

In addition, additional reinforcing layers on the surface of infilled walls also were considered could to control the damage of the walls. Sevil et al. (2011)proposed using steel fiber reinforced mortar (SFRM) to reinforce hollow brick infill walls into strong and rigid infills. Its ease of construction makes SFRM layer a frequently used damage control technique for the infilled walls of RC frames, despite the higher cost of fiber reinforced materials (Yaman2014; Erol et al. 2016). Ferro-cement jacket reinforced with welded steel mesh (Mander1994), and Epoxy-bonded fiber-reinforced polymer (FRP) laminates (Hamid2005; Triantafillou1998) also were proposed to enhance the strength of masonry infilled walls. Preti et al. (Preti et al. 2016; Preti et al. 2018; Preti et al. 2019) proposed partitioning infill earthen masonry walls by horizontal wooden planks that allow a relative sliding between the partitions. The combination of the deformability of earthen masonry and the sliding mechanism occurring along the wooden planks made the walls have a high ductility capacity during their in-plane response, significantly reducing their stiffness and strength at the same time compared with traditional solid infills.

Expect for the experimental studies mentioned above, many numerical studies were conducted to study the seismic performance of RC frames with infilled walls. Bartolomeo et al. (2017) proposed an alternative plane macro-element approach for the seismic assessment of infilled frames. The approach validation was focused on recent experimental and numerical results that investigate the influence of non-structural infills. Caliò and Bartolomeo (Ivo 2014) presented a macro-modeling approach for the seismic assessment of infilled frame structures, and the interaction between the frames and infills was simulated. Dhir et al. (2021) developed a novel computational modeling strategy using ABAQUS to investigate the in-plane behavior of RC frames with infilled walls and rubber joints. They also proposed a masonry hollow brick to reduce damage to infilled RC frames and pointed out that the frames tended to a stable load-displacement relation because most of the seismic energy was dissipated by the relatively weak masonry infills. However, to improve the collapse resistance of MHB infills in the RC frames at the large displacement stage, previous research (Cai and Cai 2017) suggested several measures such as sufficient connection rebars at the bottom of the frame beams and the ends of the infilled walls (1/3 column height). Moreover, a lightweight concrete panel could be a good potential infill to get a higher wall-collapse resistance in the MHB-filled RC frames according to the full-scale tests conducted by the authors of the paper (Cai and Su 2019). The MHB-filled RC frames performed a reasonable and stable lateral resistance behavior and ultimate capacity under an earthquake.

In summary, previous studies have mainly focused on strengthening infilled walls, separating the filled wall from structural frames and adding dampers to reduce damage. These measures improved the seismic performance of the filled walls under earthquakes to a certain extent and reduced wall damage and collapse. However, the strengthening of infilled walls may increase the additional adverse impact on the seismic performance of RC frame structures. The idea of adding energy-consuming or damping devices comes from the concept of structural earthquake resistance and effectively reduces wall damages by increasing the damping of the filled walls. However, its structures and construction process are usually complicated and expensive, which limits its widespread use. The separation of infills from frame beams and columns is mainly to reduce the strut effect of infilled walls under reversed loads caused by earthquakes, however, its waterproof and sound insulation performance is considered to be slightly poor. As a hollow lightweight material, MHB has the potential to be an ideal filling material for infilling walls in RC frames for its better sound insulation and heat preservation. To reduce the damage of the MHB infilling walls in RC frames under earthquake attack, a rigid connection for the structural measure of the MHB infilled walls with sliding layers is introduced here to replace the traditional rigid connection of MHB walls by using the ideal sliding failure modes of walls. The objectives of this paper were to investigate experimentally and numerically the effect of MHBs infilled walls with sliding layers on the seismic behavior of infilled RC frames and comprehensively compare different damage control methods. Through a finite element analysis, a detailed discussion of experimental and numerical results of full-scale MHB-filled RC frames was presented, and a comparative study of control methods was provided.

2 Experimental program

2.1 Test specimens

All tested specimens are full-scale one-bay-one-story MHB-filled RC frames designed as per Chinese design codes (Ministry2002; Ministry2010). The details of dimensions and reinforcement of the frames are plotted in Fig. 1. The sectional dimensions of the columns were 400 × 400 mm ($b \times h$), while that of the beams was T-shape with the dimension of 200 × 450 × 1000 ×100 mm ($b \times h \times b_f \times t_f$). The base beams used a larger section with a dimension of 500 × 600 mm ($b \times h$), as shown in Fig. 1. Six 16 mm deformed bars, four 16 mm deformed bars, and six 16 mm deformed were used as the longitudinal reinforcements in the frame columns, frame beams, and base beams, respectively. The steel stirrups of the frame beam, columns, and base beam all were 8 mm diameter plain rebars with a spacing of 200.0 mm and 135-degree hooks. The connection rebars were planted into the

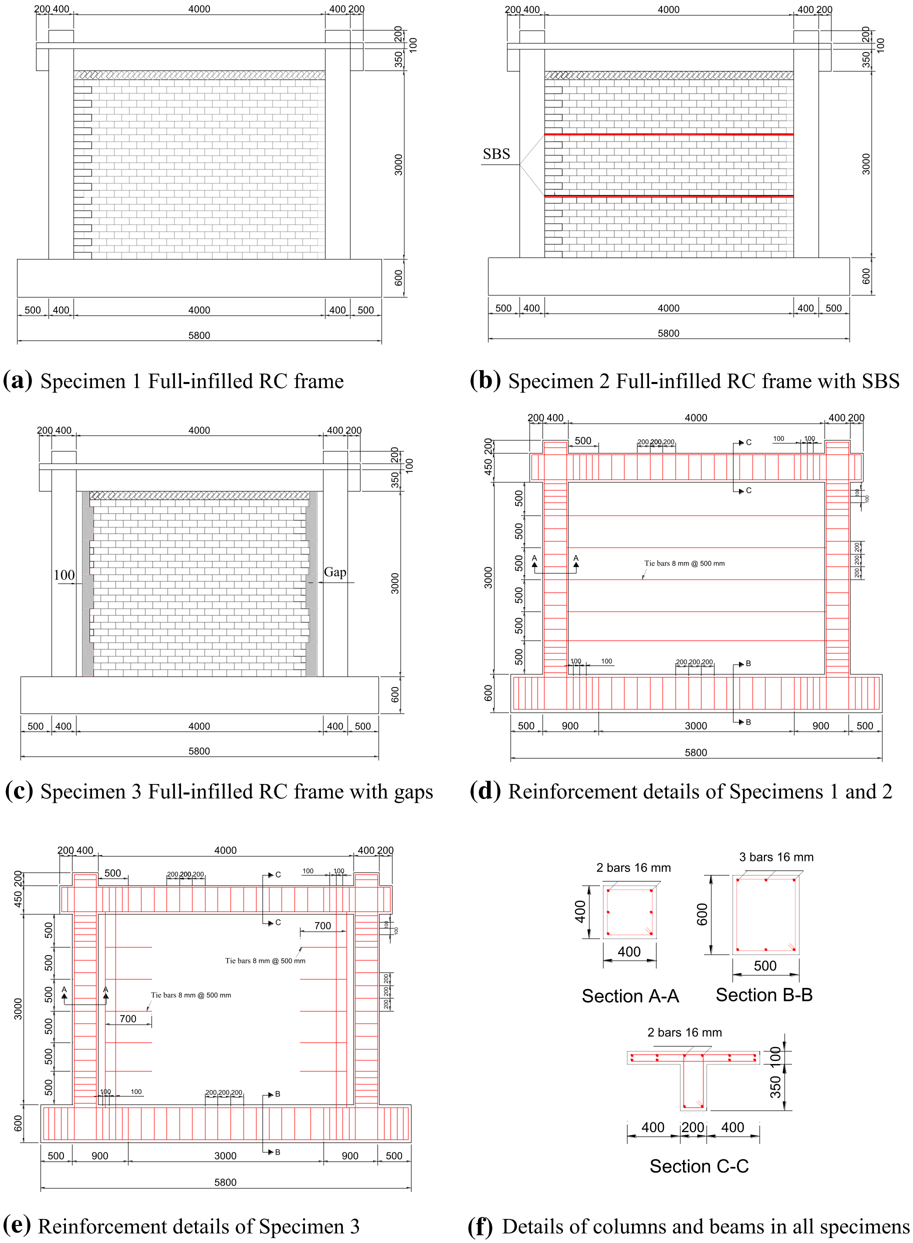

(a) Specimen 1 Full-infilled RC frame **(b)** Specimen 2 Full-infilled RC frame with SBS **(c)** Specimen 3 Full-infilled RC frame with gaps **(d)** Reinforcement details of Specimens 1 and 2 **(e)** Reinforcement details of Specimen 3 **(f)** Details of columns and beams in all specimens

Fig. 1 Dimensions and reinforcement of the tested frames

wall and connected with frame columns, as shown in Fig. 1b and d. The aspect ratio of all walls, l_w/h_w (l_w and h_w are the length and height of the walls), was 1.33.

Specimens 1 and 2 were infilled fully with MHB walls connected with ten full-length horizontal connection rebars at five levels, which include two 8.0 mm diameter plain bars at each level with the same spacing and were fixed in the mortar layer between the bricks.

In Specimen 2, two SBS slip layers were arranged inside the infilled wall with the same spacing from the wall bottom. The SBS layers were placed between the bricks without mortar. Specimen 3 applied ten horizontal connection bars, divided into 5 levels (spacing = 700.0 mm), where each level had two plain bars (diameter = 8 mm) with the same spacing from the wall bottom. All rebars were fixed in the mortar layers between the bricks. Two full separation gaps were designed between the filled wall and the frame columns in the direction of wall height, with a width of 100.0 mm, as shown in Fig. 1c. In addition, to prevent the wall from collapsing prematurely due to the two gaps during the test, two detailing columns were constructed on both sides, which were staggered by MHBs and their longitudinal reinforcements passed the holes of bricks filled by mortar.

All frame beams and columns were made of normal compressive strength concrete. The average cube compressive strength of the used concrete (size $100 \times 100 \times 100$ mm^3) was 33.5 N/mm^2 (prismatic concrete compressive strength, $150 \times 150 \times 300$ mm^3, 14.3 N/mm^2), whose elastic modulus was 30.0 kN/mm^{2}obtained by standard tests (Ministry 2002; Ministry 2010). For the longitudinal and transverse reinforcements, the yield strength of the used 8 and 16 mm diameter plain rebars were 480 and 420 N/mm^2 (State 2018), respectively. The frames were infilled with MHBs ($240 \times 200 \times 110$ mm, see Fig. 2), which are the same as the bricks in the literature (Cai and Cai 2017), (Cai and Su 2019). The ratio of net area to the gross area of the bricks was 47.85%, and the average weight per unit of the bricks was about 4.96 N. The thickness of mortar used for the walls was between 7 and 10 mm. The average compressive and tensile strengths of the mortar used in all frame specimens were 5.62 and 0.45 N/mm^2, respectively, through standard tests (Ministry 2009). The average compressive strength of the used masonry brick in the direction of its holes was 3.5 N/mm^2, considering the gross area of the bricks. The SBS layer is made of polyester felt, glass fiber felt, and glass fiber reinforced polyester felt as the base, and asphalt using a modifier of SBS. Its thickness and density were 3.0 mm and 34.3 N/m^2 respectively, and covered with polyethylene film as isolation materials, as shown in Fig. 2. The dissoluble composite of the membrane of the SBS layers was 2100 g/m^2 and its elongation at maximum tensile force can be over 35%. The maximum tensile force load along the length direction of the layers (test specimen length 200 mm and width 50 mm) was 3.33 N/mm^2.

2.2 Test setup and load history

The details of the test setup and instrumentations are presented in Fig. 3. The base beams of the specimens were fixed to a strong floor through several high-strength steel bolts. Each specimen was tested under a combination load with reversed cyclic lateral load and a

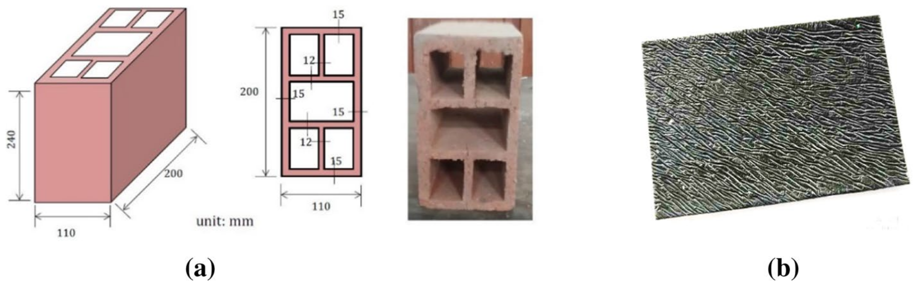

Fig. 2 Applied bricks and sliding layers in tested specimens **a** Masonry hollow bricks, **b** SBS layer

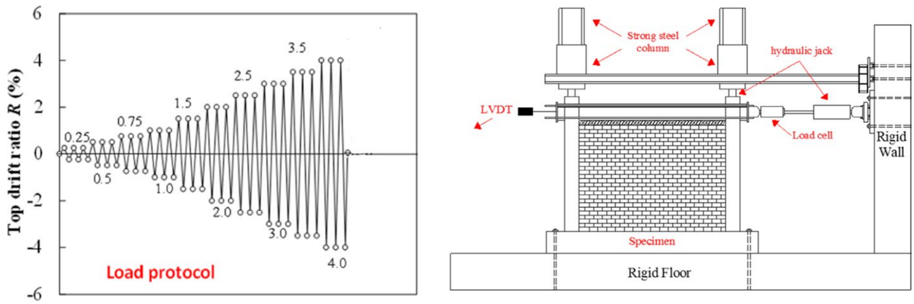

(a) Load history (b) Testsetup

Fig. 3 Loadprotocol and test setup

constant axial load. The lateral load was applied at the upper frame beams using a hydraulic jack shown in Fig. 3, while the axial load was applied at the top of the columns by two hydraulic jacks. The applied axial load in each column was 572.0 kN, about 25% of the axial load capacity of the columns calculated based on concrete prismatic compressive strength. To confirm the possible move of the specimens during the tests, two linear variable differential transducers (LVDTs) were used at the ends of the base beams. One LVDT was applied at the load level to measure the lateral displacement of the specimens to calculate the drift ratio of the specimens (R) to control the lateral loading.

As shown in Fig. 3, a reversed cyclic lateral load was conducted at the top frame beam of each specimen, after the designed axial load was applied on the top of the two frame columns. To observe the first crack of the infilled walls, the loading method at the beginning of the test is designed to be force-controlled until the drift rate was 0.25%, in both directions. Afterward, three full cycles of displacement-controlled loading were conducted at the subsequent target loading cycles until the drift ratio was 4.0%. The main test observations included cracking, damage, and collapse of the bricks, all of which were carefully recorded during the tests. The tests were ended when (1) the drift ratio reached 4.0% to ensure the safety of researchers and test devices, or (2) the frame failed to resist the applied loads making the load-carrying capacity below 50% of the peak load.

3 Experimental results

3.1 General observations

As shown in Figs. 4, 5, and 6, the treatment methods in the walls present a significant influence on the seismic performance of infilled RC frames. For Specimen 1, when the drift ratio was 0.25%, several cracks were observed, including diagonal and horizontal cracks on both sides of the wall, transverse cracks in the middle of the frame columns, and the diagonal zone at the ends of the frame beam (upper beam, same as below). When R reached 0.5%, new cracks appeared inside the frame columns and were roughly distributed on the infilled wall. The previous cracks at the ends of the beam extended to the beam edges and the beam-column joint zones. While R was 1.0%, several cracks were observed in the mortar in the middle of the wall and the zones of the connection rebars. Some connecting steel bars were exposed and the mortar layer is

(a) front view of wall collapse **(b)** back view of wall collapse

Fig. 4 Damage of specimen 1 at R = 4.0%

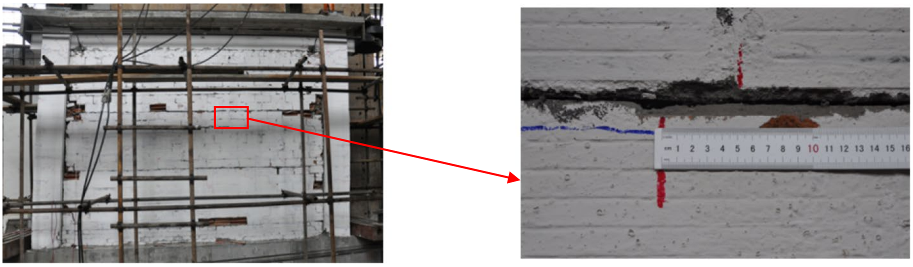

(a) overall damage at R=4% **(b)** slippage of SBS layer at R=2%

Fig. 5 Overall damage of specimen 2 andslippage of the SBS layers

Fig. 6 Damage of specimen 3 at R = 4%

completely peeled off. The mortar on the wall's middle sides fell off and the upper connection bars were slightly bent outside when R reached 1.5%, and several bricks were crushed and fell off on both sides of the wall at the same time. When R was 2.0%, the cracks in the columns developed significantly, while the connecting rebars were bent seriously and the bricks continually fell off from R = 2.5%. After R exceeded 3.0%, the wall top was separated from the upper beam bottom, and more connecting bars were exposed. Before R = 3.50%, the wall subsidence occurred in the specimen middle, and more bricks were crushed and more connecting rebars were seriously bent. At R = 4.00%, the infilled wall collapsed almost completely, as shown in Fig. 4a, making the wall exhibit a similar structural behavior to a bare RC frame.

Regarding Specimen 2, as shown in Fig. 5a, the useof SBS layers significantly reduced the damage and collapse of the infilledwall. At R = 0.25%, several cracks were observed along the SBS layers, at thebottom corner of the wall, the middle and bottom of the columns, and the end ofthe frame beam. When R reached 0.50%, the wall was divided into three parts bythe two SBS layers, and the previous cracks were developed slowly until R = 1.0%.From R = 1.25%, the SBS layers started to slide freely in the wall. In general, thecracks and damage to the wall were much smaller than those of Specimen 1. Majorcracks and damage were concentrated on thetwo bottom edges of the wall. The corner bricks and beam bottom concrete were crushed and the internal longitudinalreinforcements were exposed in the beam. After R = 1.75%, several cracks appearedon the columns and the wall sides. When R = 2.00%, only the bricks at the corners of the three small walls were crushed. This means that the diagonalresistance structs were formed in each small wall. However, due to slippage of theSBS layer, the diagonal struct was weak and insufficient to form diagonalcracking damage. The three small walls separated by the layers continued toslide along the layers. As shown in Fig. 5b, the slip displacement reached50.0 mm at R = 2.0%. After R exceeded 3.0%, the three small walls continued toslide, as well as the bricks were crushed, fell off, and expanded horizontallyuntil the end of the test. The cracks extended at the beam ends and the bottomof the columns, but the wall was intact with less damage compared with Specimen1.

For Specimens 3, several diagonal cracks occurred in the wall and developed rapidly at the beginning. When R reached 0.50%, the bricks at the top of the wall fell off and some cracks were observed between the wall and the columns, at the frame beam ends. When the drift ratio reached 0.75%, more bricks fell off and were crushed at the inside edge of the columns, and the previous cracks were developed quickly. The beam-column joint zones were damaged and local concrete fell off at the same time. When R exceeded 1.0%, all cracks observed previously were developed further and new cracks appeared in the middle of the columns. The collapsed area of the wall was increased and concentrated near the ends of the columns, but the collapse ratio was still small until R = 1.25%. At R = 1.50%, the large increase in the cracks and collapsing in the middle of the wall was not obvious because the wall was separated from the detailing columns. From that moment on, the frame behaved as a bare RC frame. When R = 1.75%, the wall was damaged slightly, the concrete at the beam bottom was crushed, and the steel rebars of the columns were buckled slightly. After that, the rebars of the columns were severely buckled and the concrete at the beam ends was crushed heavily as well. As R reached 2.50%, several steel rebars of the columns were broken, while the rebars of the frame beam were severely buckled. The infilled wall was in close contact with the frame columns on both sides at R = 3.0%, and the longitudinal steel rebars at the beam ends were fractured, leading to the final failure of the frame at R = 4.0%. In summary, all described cracks and damages were distributed in the infilled wall and several bricks fell off from the frame, however, the wall was intact and the frame was protected well, as shown in Fig. 6.

3.2 Hysteretic behavior and skeleton curves

The lateral load-displacement hysteretic curves of all specimens and their skeleton curves are presented in Fig. 7, which both are important to assess the seismic behaviors of the specimens. The results show the load-carrying capacity of the specimens is greater than that of the bare frame made with the same bricks in the previous study (Cai and Cai 2017). Due to the influence of the infills, the skeleton curves of Specimens 1 and 3 present distinct peaks (See Fig. 7a, c, d). After adding the SBS layers to Specimen 2, the strut effect of the infilled wall was significantly weakened and the skeleton curve did not present an obvious peak (see Fig. 7b). As shown in Fig. 7c, the hysteretic curve of Specimens 3 was firstly a vertical long-narrow shape but rapidly changed to a long-fat shape. Besides, the curve appeared a sudden increase in load-carrying capacity when R reached 2.5%. The closing of the gaps on both sides of the wall was the main reason for the increase in the capacity. The skeleton curves plotted in Fig. 7d show that the skeleton curve of Specimen 1 increases to

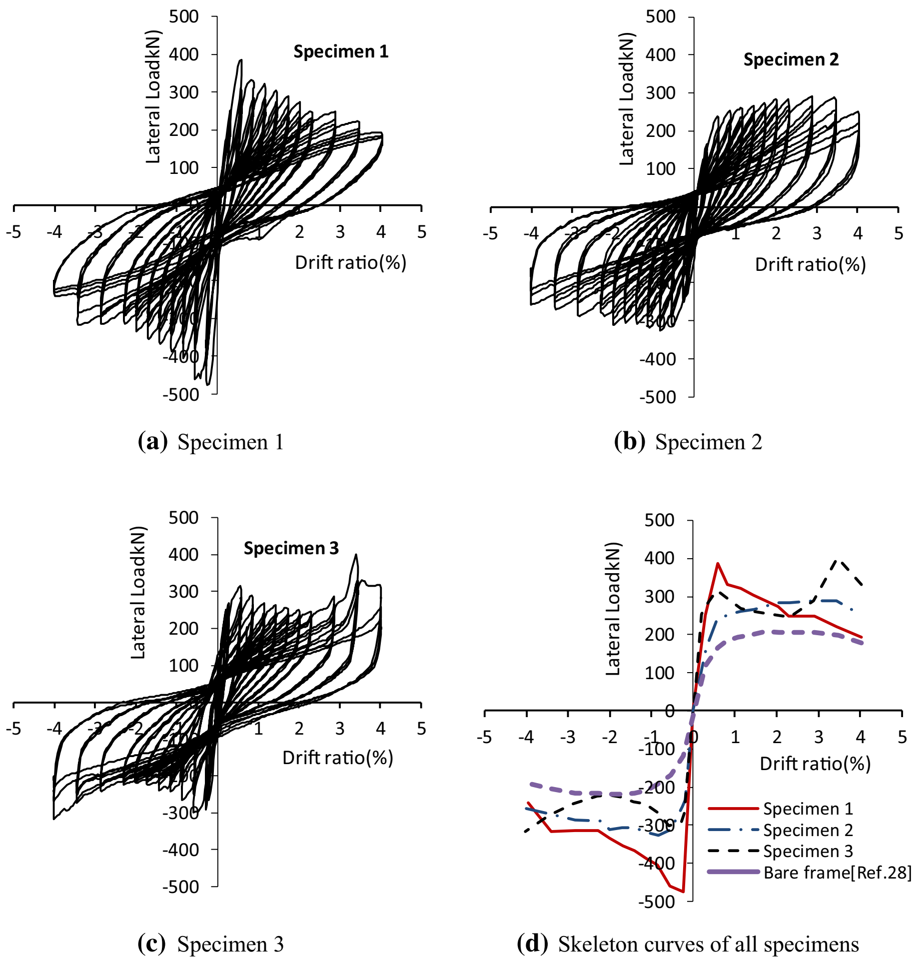

Fig. 7 Lateralload-displacement curves oftested specimens

its maximum capacity at R = 0.50% and then decreases sharply until about 2.0%, followed by a short stable stage until R = 3.0%. Besides, compared with Specimen 1, the curve of Specimen 2 was more stable in increasing and decreasing phases in both directions. However, both the maximum load-carrying capacity and initial stiffness were smaller than those of Specimens 1 and 3, especially its maximum capacity was only 3/4 times that of Specimen 1. For Specimen 3, the curve reached the first peak load at R = 0.50%, then slowly declined with a similar downward trend to that of Specimen 1 and ended at R = 2.0%. After that, the load-displacement curve increased to its second peak load when R reached 3.0–4.0%, which was larger than the first peak load. As the lateral displacement increased, the lateral load dropped sharply to a similar level to those of the other two specimens. With the lateral load increasing, the bending and damage of the detailing columns increase continuously, and its load-carrying capacity decreases gradually. As the detail columns bent causing the gaps between the wall and detailing columns to be closed, the bearing capacity increased gradually. After that, the bearing capacity decreased again and a second peak occurred as the wall damage intensifies. It was understood that Specimen 3 reached its ultimate load (the first peak) at R = 0.5%, however, the specimen provided a higher load-carrying capacity because the detailing columns made the wall contact with the frame columns, further increasing the ultimate capacity of the specimen. Compared with Specimen 1, Specimen 3 provided a small early peak capacity because the gaps between the frame and infilled wall reduced the diagonal strut effectiveness of the infills. But after the gaps were closed at the corners, Specimen 3 could provide almost the same level of capacity as Specimen 1 at the same displacement.

3.3 Ductility, stiffness, and energy dissipation

3.3.1 Initial stiffness and ductility

The initial stiffnesses discussed in this study include mainly initial elastic deformation stiffness K_{int} and yielding stiffness K_y, as shown in Fig. 8. The stiffnesses were calculated as secant displacement stiffness corresponding to 0.33 and 1.0 times the measured yielding displacement (Δ_y) of the specimens, respectively. The yielding displacement was the measured displacement corresponding to (1) the yielding point of the skeleton curves of the load-displacement curves

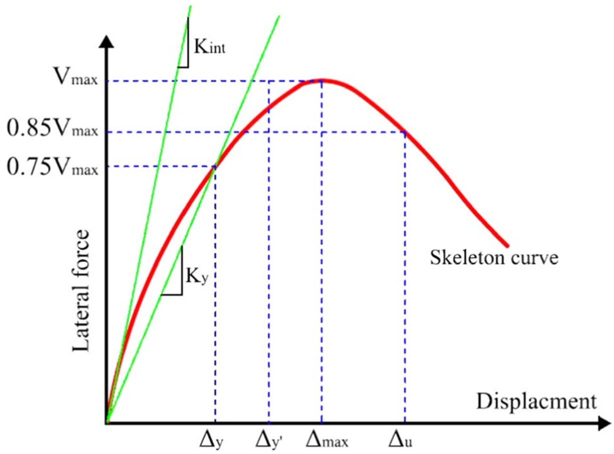

Fig. 8 Definition of ductility and stiffness on the skeleton curves

of the elements or (2) when certain longitudinal rebar in the frame columns reached its yield strength. In the present study, taking the yielding displacement Δ_y of the infilled frames as the measured displacement corresponding to 0.75 V_{max}, and using maximum lateral displacement (Δ_{max}) and ultimate displacement (Δ_u) corresponding to 85% V_{max} (Paulay 1992; Pam 2001), the maximum and ultimate ductility of the frames (μ_{max} and μ_u) are calculated as Eq. (1). The ultimate drift ratio δ_u was calculated using the ultimate displacement divided by specimen height (H), which is calculated as Eq. (2).

$$\mu_{\max} = \frac{\Delta_{\max}}{\Delta_{y\prime}} \quad \mu_u = \frac{\Delta_u}{\Delta_{y\prime}} \quad \Delta_{y\prime} = \frac{4}{3}\Delta_y \tag{1}$$

$$\delta_u = \frac{\Delta_u}{H} \times 100 \tag{2}$$

Table 1 lists the main experimental results of all specimens. Compared with Specimen 1, the other specimens presented a higher ductility. In Specimen 2, the sliding layers reduced the damage of the infilled wall because the layers separated the wall into three small walls with diagonal struts avoiding the damage of the central wall at the post-peak stage. This also resulted in mitigation in the degradation of the load-carrying capacity at the stage. However, due to the low elastic property of the SBS layers, the initial stiffness of Specimen 2 was smaller than that of the other specimens. The high ductility of Specimen 3 was because the gaps released the deformation of the wall. The specimen also exhibited the highest initial stiffness as the detailing columns made the frame have larger structural integrity at the initial stage.

3.3.2 Energy dissipation capacity

The equivalent viscous damping coefficient (h_{eq}) defined by previous research (Jacobsen 1960) was applied in this study to discuss the energy dissipation capacity of the specimens. Figure 9 presents the development of the h_{eq} coefficient-drift ratio curve of all specimens. The results indicate that the infill properties, gaps, and the sliding layer all have a significant influence on the energy dissipation capacity of the frames, especially at the early stage of loading. Because the sliding layer reduced the diagonal strut action of the infills, the self-restoring capacity of the infilled RC frame was increased resulting in a significant decrease in the energy dissipation of Specimen 2. Besides, the additional gaps near the frame columns only influenced the energy dissipation capacity of the frame at the large deformation stage, as shown in Fig. 9. Compared with the bare RC frame in the literature (Cai and Cai 2017), an obvious decrease in the factor h_{eq} was observed in Specimen 1, in particular before the drift ratio reached 2.0%. The additional SBS layers made the energy dissipation capacity of the RC frame (No. 2) higher than that of the bare RC frame (Cai and Cai 2017) before R = 3.0%, but a similar energy dissipation capacity was presented at the subsequent loading cycles.

3.3.3 Lateral residual deformation

The lateral residual deformation of structural elements represents their self-resilience capacity affecting the repair and strengthening of whole structures. In general, a RC frame is expected to recover for an easy repair after an earthquake, but the damage and

Table 1 Summary of results of test specimens

Specimens	$V_{max}{}^{a}$ (kN)	$V_{max}{}^{b}$ (kN)	K_{int} (kN/mm)	K_y (kN/mm)	Δ_y (mm)	Δ_{max} (mm)	Δ_u (mm)	μ_{max}	μ_u	δ_u (%)
1	387.34	476.18	26	22.06	12.55	19.57	48.98	1.17	2.93	1.52
2	290.14	327.02	16.39	12.13	16.24	95.58	135.50	4.41	6.26	4.20
3	403	317	35.52	9.89	16.14	114.06	130.32	5.30	6.06	4.04

[a]Push direction, and [b]Pull direction

Fig. 9 Equivalent viscous damping coefficients vs. drift ratios

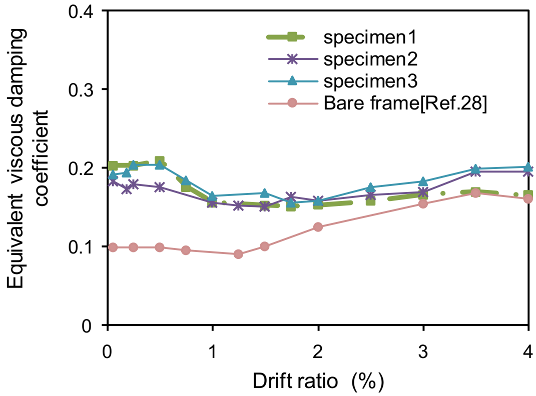

plastic deformation accumulated on infilled walls during reverse lateral loads usually prevent RC frames from recovering. In this study, the residual drift ratio (R_{res}) of columns was the drift ratio corresponding to the lateral load equaling zero at the first loading loop with each target drift ratio. The calculated ratios were taken as the mean values obtained in both load directions in the study, which are presented in Fig. 10. The results show that the residual drift ratios of all specimens increase stably with the target drift ratios. Specimen 1 presents the highest residual deformation as the wall was damaged significantly caused by the development of cracks and the strongest diagonal strut effectiveness in the fully infilled frame. While both Specimens 2 and 3 show almost the same behavior which means both the SBS layers and the gaps at both sides of the wall reduced the diagonal strut effect of the infills on the surrounding frame columns. This significantly increased the restoring of the frame columns and beams, which is similar to a bare frame, especially at the large deformation stage. The difference in the residual deformation caused by the different lengths of connecting rebars just can be observed before R = 2.0%, which may be attributed to the anchorage of the connecting rebars failing at the large deformation stage.

Fig. 10 Evolution of residual deformation of the frames

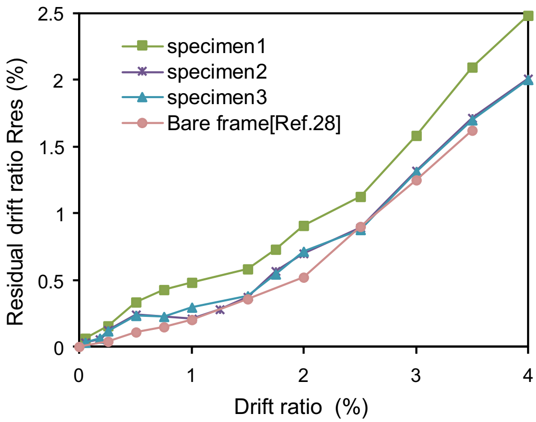

3.4 Failure modes of infilled RC frames

The failure modes of the infill walls used the masonry bricks mainly include corner crushing failure (CC), sliding shear failure (SS), diagonal compression failure (DC), diagonal cracking failure (DK), and frame failure (FF), as same as previous research summarized in Fig. 11 (El-dakhakhni 2003). Based on the experimental results, the failure modes of Specimens 1 to 3 are CC, SS, and CC modes, respectively.

The CC and DC failure modes are prone to occur in relatively strong RC frames with weak infill walls or RC frames with large aspect ratios. The MHBs or other lightweight blocks are used increasingly recently due to their suitable strength, which can produce the suitable diagonal strut effect of the infill wall in RC frames at the early stage of deformation. The CC and DC are the most common failure modes of infilled walls in China. When thin flexible layers are arranged in the horizontal brick joints of the hollow brick infill wall such as the SBS layer used in the study, the SS failure mode usually occurs in RC frames. Besides, the DK mode usually occurs when the frames or beam-column joints are relatively weak with a quite strong infill. It is worth mentioning that only CC and SS failure modes are of practical importance (Du Beton 1996), while the DK mode occurs very rarely because solid bricks with high strength are no longer used in infilled walls in many countries such as China. Generally, the frames with DK failure modes can absorb more earthquake energy, however, their damage is much more serious than other frames. On the contrary, the damage of infilled walls in RC frames with FF failure mode is much smaller, but the frame joints are usually damaged seriously. It can be seen that the walls with SS, DC, and CC failure modes can effectively protect structural frames at the cost of serious damage to the infilled walls (except SS mode). This highlights the superiority of the treatment method in Specimen 2 with SS failure mode.

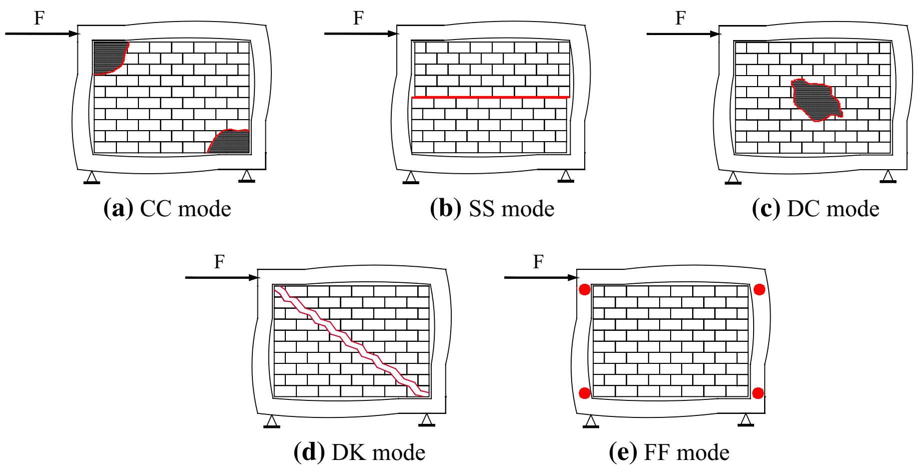

Fig. 11 Different failure modes of masonry-infilledframes

4 FEM simulation

4.1 Modeling strategy

A commercial finite element method (FEM) analysis software *ABAQUS* was used to model the masonry infilled frames. Because the infilled wall was isolated from Specimen 3, which meant that the specimen was considered to be a bare frame to a certain extent, it was not simulated in the study. Specimens 1 and 2 were applied for optimizing FEM models working as two controlling specimens for the discussion below.

The three-dimensional 8-node solid element, C3D8R, was used to model the concrete frames, masonry units, and sliding layer (i.e. SBS layer, Basalt fiber-reinforced polymer (BFRP) laminate, and steel plate). The beam element (B31) was applied to model the steel reinforcements in RC frames and connection rebars in the infills of RC frames, which presented with an elastic-plastic material response. The Concrete Damaged Plasticity (CDP) model was applied to identify the non-linear behavior of concrete, in which the main failure was assumed as compressive crushing and tensile cracking (Carreira1985), (Carreira1986). Figure 12 shows the constitutive model applied in the study for the concrete materials under tension and compression.

Besides, the concrete model used a Druker-Prager strength hypothesis modified by Lubliner et al. (1989), and Lee and Fenves (1998). For this, the failure surface in the deviatoric cross-section was determined by Parameter K_c. It is always greater than 0.5, and the deviatoric cross-section of the failure surface becomes a circle (as Drucker-Prager strength hypothesis) when K_c is 1.0. The study used the original CDP model recommend value assuming K_c as 2/3 (Abaqus 2011). For this value, the shape is similar to the strength index (a combination of three mutually tangent ellipses) formulated by William and Warnke (William 1974), which is a theoretical-experimental index based on tri-axial stress test results, as shown in Fig. 13a. In addition, the plastic is adjusted by eccentricity (plastic potential eccentricity) in the CDP model, which was taken as 0.1 referring to the literature, which means the surface in the meridional plane becomes a straight line(Carreira 1985). As shown in Fig. 13b, the dilation angle in the CDP model was interpreted as a concrete internal friction angle, which was assumed as 36° according to the literature (Carreira 1985). Besides, the viscosity parameter, μ, was ignored in Abaqus/Explicit analysis and was set as 0.0 (William 1974). Figure 13c shows the constitutive behavior of the concrete materials under biaxial stress. Here, the ratio of the strength in the biaxial to the strength in the uniaxial σ_{b0}/σ_{c0} (f_{b0}/f_{c0})was taken as 1.16 (William 1974).

The masonry units were treated as continuum elements and modeled by the Drucker Prager plasticity model in ABAQUS, an inelastic constitutive model. In this study, a compression hardening masonry continuum brick model was used, whose main material properties are listed in Table 2.

The same SBS layer, BFRP laminate, and steel plate were used as the sliding layers in infilled masonry walls for comparative study, which all were considered elastic materials. The Young's modulus and Poisson's ratio as well as the coefficient of friction between bricks and the layers are listed in Table 3. Besides, the material properties of steel rebars are summarised in Fig. 14. The total deformation, ε, is described as equal to the sum of elastic deformation (ε^{el}) and plastic deformation (ε^{pl})

The coherent behavior methodology was used to determine the brick-to-brick and brick-to-frame interaction in this paper. The surface-based cohesive behavior provides a simplified way to model cohesive connections with negligibly small interface

Table 2 Material properties for continuum bricks and mortar

Properties	Parameters	Value
Elastic	Density (kN/m^3)	1900
	Modulus elasticity (N/mm^2)	20,000
	Poisson ratio	0.15
Inelastic properties	Angle of friction	46°
	Flow stress ratio	0.8
	Dilatation angle	20°

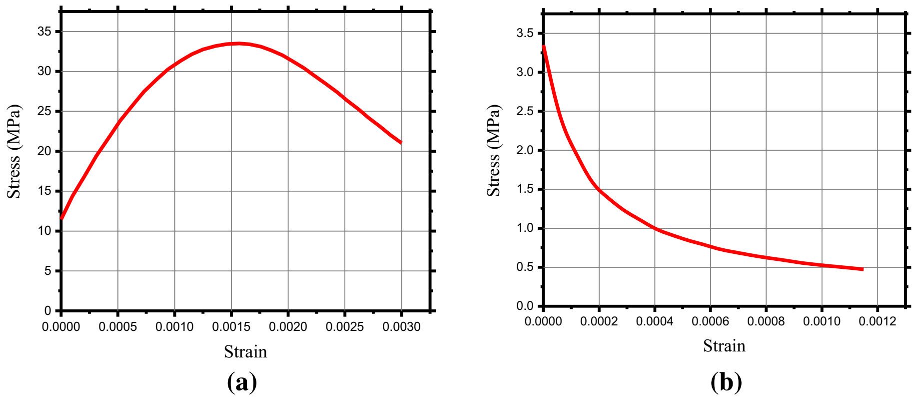

Fig. 12 Constitutive models of concrete **a** under compression and **b** tension

Table 3 Material properties of sliding layers

Parameters	SBS layer	BFRP laminate	Steel plate
Density (kN/m^3)	1240	2920	7850
Modulus elasticity (N/mm^2)	9.52	75,000	200,000
Poisson ratio	0.43	0.23	0.3
Coefficient of friction	0.32	0.75	0.64

thicknesses, which is defined directly in terms of a traction-separation law. It is worth mentioning that cohesive behavior damage on the surface is an interaction property, not a material property (Wang 2020). Figure 15 shows that in the masonry portion describing the mesoscale model, the size of the units has to be expanded by the mortar thickness h_m in both directions. A linear elastic traction separation behavior was assumed in the interaction model followed by the initiation and evolution of the damage. The nominal traction stress vector, {t}, was determined by three components: a normal stress value (t_n) in the perpendicular direction on the cohesive behavior surface, and two transverse shear stresses (t_s and t_t). The elastic behavior is given as,

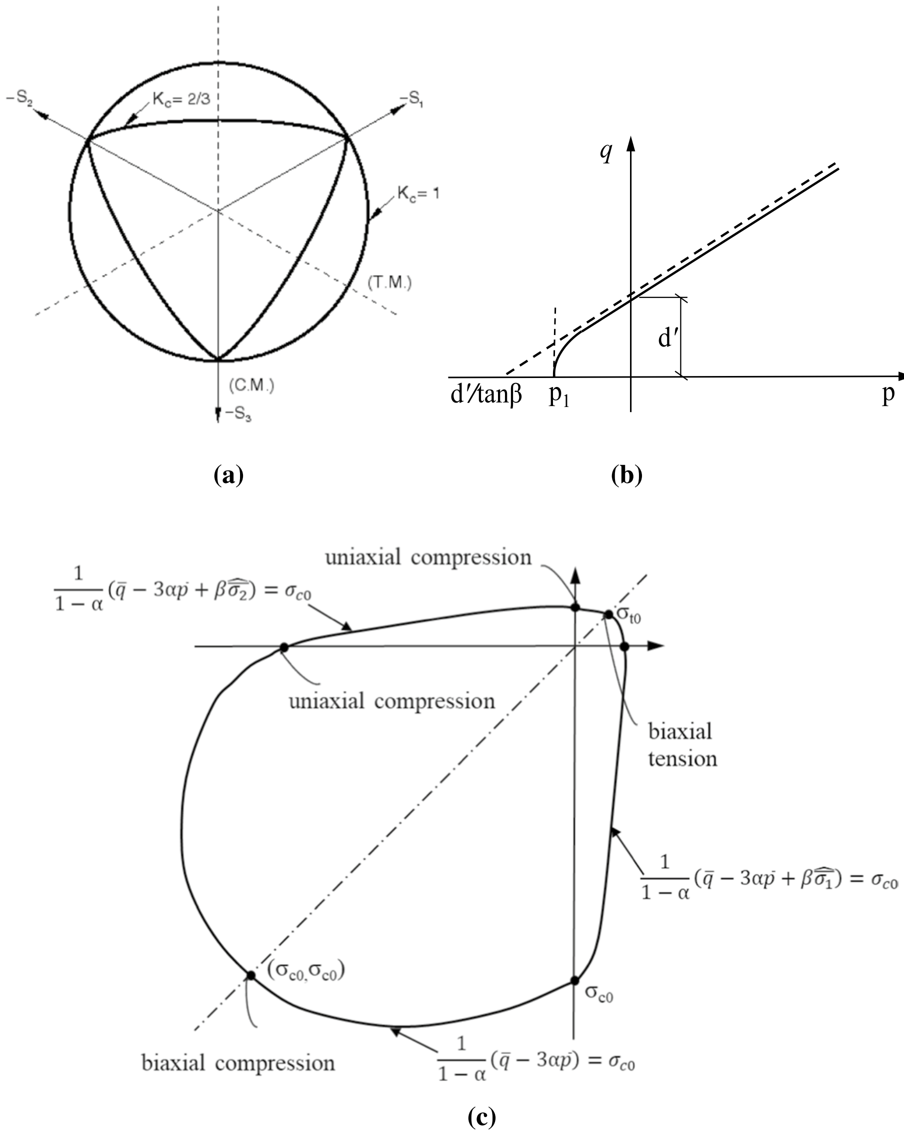

Fig. 13 **a** Deviatoric cross-section of failure surface **b** hyperbolic surfaceof plastic potential in the meridional plane **c** constitutive model of concreteunder biaxial stress

$$t = \begin{Bmatrix} t_n \\ t_s \\ t_t \end{Bmatrix} = \begin{bmatrix} K_{nn} & K_{ns} & K_{nt} \\ K_{ns} & K_{ss} & K_{st} \\ K_{nt} & K_{st} & K_{tt} \end{bmatrix} \times \begin{Bmatrix} \varepsilon_n \\ \varepsilon_s \\ \varepsilon_t \end{Bmatrix} = K \times \varepsilon \tag{3}$$

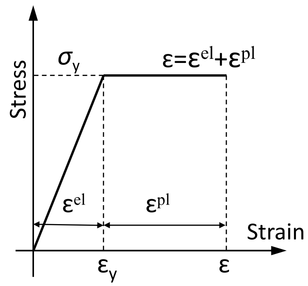

Stages	Parameters	Longitudinal rebars in columns	Transverse rebars in columns	Connection rebars in the walls
Elastic stage	Density (ton/mm³)	7.85E-9		
	Elastic modulus (N/mm²)	200000		
	Poisson ratio	0.30		
Plastic stage	Yield stress (N/mm²)	420.0	480.0	350.0
	Hardening coefficient	0.00		

Fig. 14 Material model of steel materials

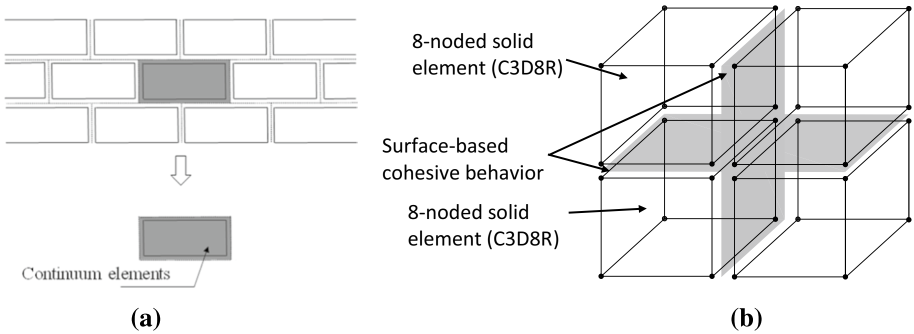

Fig. 15 Models of masonryunits and the interfaces **a** Masonry portion describing mesoscale model **b** masonry units and surface-basedcohesive behavior

where K is the elastic stiffness matrix for fully coupled behavior. The stiffness matrix can be simplified to a diagonal matrix if the uncoupled behavior between the normal and shear behavior is considered. The normal and tangential stiffness coefficients are defined by Lourenço (1996), which are given as:

$$K_{nn} = \frac{E_u E_m}{h_m (E_u - E_m)} \tag{4}$$

$$K_{ss} \text{ and } k_{tt} = \frac{G_u G_m}{h_m (G_u - G_m)} \tag{5}$$

where E_u and E_m are Young's moduli of the masonry units and mortar, G_u and G_m are their corresponding shear moduli, respectively. h_m is the actual thickness of the joints, the 10 mm thick mortar joints are assumed for this purpose. The stiffness values obtained from the equations do not correspond to a penalty contact method, which means that the overlap of adjacent units becomes obvious under compression. This is a phenomenological description of masonry crushing because the failure process in compression is described by the microstructure of units and mortar and the interaction between them. In this study, the calculated values of K_{nn}, K_{ss}, and K_{tt} are 222 , 99 and 99 N/mm^3, respectively. When the

Table 4 Comparison between simulated and experimental results

Specimen	$K_{ini(FEM)}$ (kN/mm)	$K_{ini(EXP)}$ (kN/mm)	$K_{ini(FEM)}$/ $K_{ini(EXP)}$	$P_{ult(FEM)}$ (kN)	$P_{ult(EXP)}$ (kN)	$P_{ult(FEM)}$/ $P_{ult(EXP)}$	$\Delta_{ult(FEM)}$ (mm)	$\Delta_{ult(EXP)}$ (mm)	$\Delta_{ult(FEM)}$/ $\Delta_{ult(EXP)}$
1	32.31	38.45	1.19	361.34	420.12	0.86	45.15	36.76	1.23
2	19.26	16.39	1.18	271.76	290.14	0.94	88.61	95.58	0.93

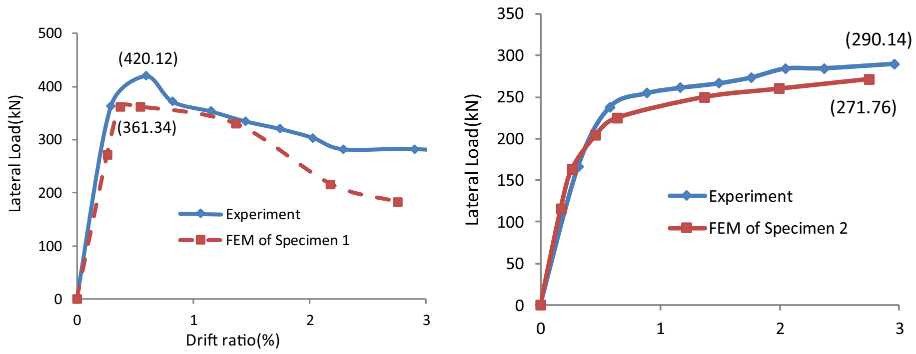

(a) Specimen 1 **(b)** Specimen 2

Fig. 16 Comparison between experimental and simulated results

damage initiation criterion is achieved based on the defined tractions between the masonry interface shear and tensile strength of the joints. The quadratic stress criterion is used to define damage initiation. This criterion is suitable when the quadratic stress ratios of masonry interfaces are equal to 1.0. The criterion was adopted as it effectively predicts the damage initiation of joints subjected to mixed-mode loadings (Campilho 2008), which is the case in masonry joint interfaces. The masonry joint interfaces are sub-subjected to tensile stress in the normal direction and shear stress in the two shear directions (Kurdo 2017).

4.2 Validation of FEM model

Figure 16 shows the comparison between the experimental curves (average values in both directions) and simulated load-displacement curves of the two control RC frame specimens. The results show that the FEM model evaluates the experimental behavior of the frames with a good agreement. The simulated results of the frame with sliding layers were 15% smaller than the experimental results after the elastic stage in both specimens. Therefore, the simulated load-displacement response of the frame was accepted, as shown in Fig. 16. Table 4 lists the comparison details of the curves, including initial stiffness (K_{ini}) determined as the slope of the initial linear portion of the curves, as well as the ultimate load and ultimate displacement (P_{ult} and Δ_{ult}). The results show that the ultimate load and displacement of both frames are evaluated well with a maximum error ratio of 14 and 23%, respectively. The initial stiffness of the frame using the SBS layers was assessed well with an error ratio of 18%.

5 Discussion on the test and FEM results

In this section, a parametric analysis using the FEM models developed above was conducted to study the failure modes and the effect of the sliding layers on the seismic behavior of the infilled frames. All analyses and discussions were based on FEM models and observed test results in the study. Table 5 shows the arrangement of the sliding layers inside the simulation specimens (Model I ~ Model IX), in which Model II is Specimen 2 tested in the study as a control specimen.

5.1 Failure modes

Figure 17 shows damaged areas for all tested and numerical specimens, while Table 6 lists a summary of the main results including the maximum load and corresponding displacement, the initial stiffness, and the failure modes of the frames. The results show that the failure modes of the filled walls change from DC or CC mode to SS mode when the sliding layers are applied inside. This was also verified by the experimental results in the study and the literature (Cai and Cai 2017). Here, Specimen R1 (RC frame 0% in Cai and Cai 2017) in previous research, a fully infilled frame without openings similar to Specimen 1, was applied here for a comparative study. The difference from Specimen 1 was that the connecting rebars were not full length and only had a length of 700 mm. The failure mode of Specimen R1 was DC + CC mode, because (1) the length of connecting steel rebars was insufficient and (2) the strength of the filled wall was low. The masonry units in the central zone of the wall were first destroyed under reversed cyclic lateral loads. The damaged area increased and extended to the diagonal zones of the frame finally to form DC + CC failure mode. However, Specimen 2 and other specimens used more than one sliding layer, the filled wall was divided into multiple parts by the layers which then weakened the diagonal strut effect in the whole infilled wall. This led to the frame being damaged with the SS failure mode. The results listed in Table 6 show that the main model of the frames with sliding layers is SS failure mode, especially when the number of layers increases. The DC mode and CC mode disappeared when the number of layers was large. Moreover, the smaller the friction coefficient of sliding layers was, the easier this effect changed.

5.2 Effects of sliding layers

To understand the effect of sliding layers on the seismic behavior and damage of the masonry infilled frames under cyclic loads, such as load-displacement response and

Table 5 Details of simulation specimens in the parametric study

Layer materials	The number and spacing of sliding layers (L_s) in the filled walls		
	One layer (L_s=1500 mm)	Two layers (L_s=1000 mm)	Three layers (L_s=750 mm)
SBS	Model I	Model II (Specimen 2)	Model III
Steel plate	Model IV	Model V	Model VI
BFRP laminate	Model VII	Model VIII	Model IX

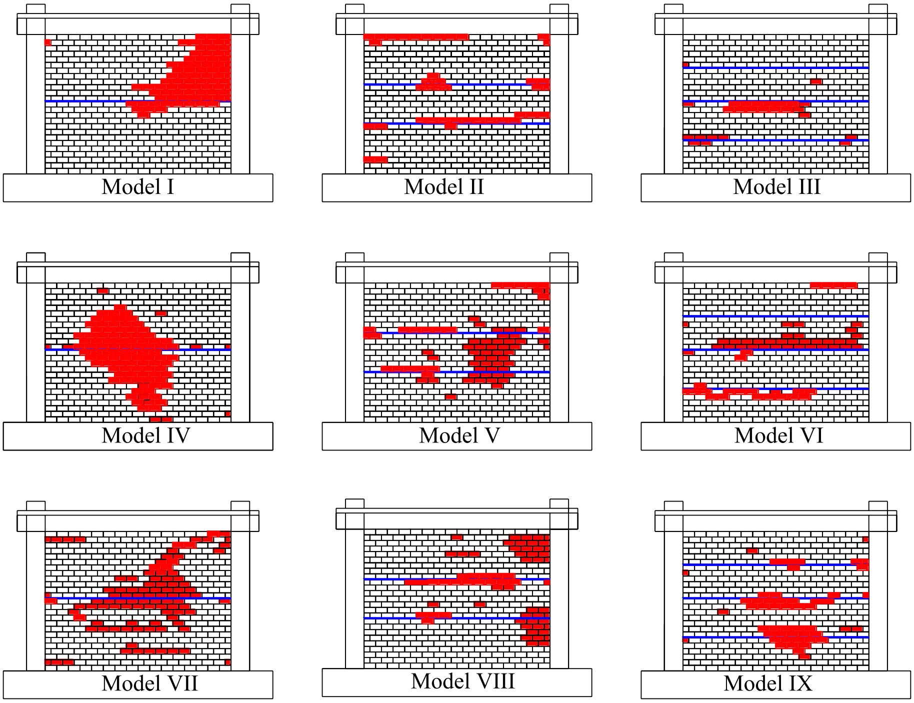

Fig. 17 Damages and collapse of the simulated specimens (Model II = Specimen 2)

Table 6 A summary of the simulated results of the FEM specimens

Specimens	Initial stiffness (kN/mm)	Ultimate loads (kN)	Ultimate displacements (mm)	Collapse ratio (Cai and Cai 2017) (%)	Failure modes
Model I	23.73	263.4	90.0	18.6	SS + CC
Model II	28.05	268.3	86.25	9.5	SS
Model III	15.45	242.3	69.88	6.38	SS
Model IV	28.80	365.9	89.70	24.88	SS + DC
Model V	29.14	331.1	71.4	17.13	SS + DC
Model VI	27.58	321.3	71.9	13.75	SS
Model VII	29.23	358.7	89.1	23.80	SS + DC
Model VIII	29.07	316.4	71.5	15.00	SS + CC
Model IX	30.86	333.4	89.2	12.03	SS

wall collapse ratio, comparative analysis based on the FEM simulation results was performed, including the effects of the spacing of the sliding layers and the materials of the layers.

(1) Effect of the spacing of the layers (L_s)

When a SBS layer is paved in the infills (Model I), the diagonal strut effect is interrupted at the sliding layer. When the number of sliding layers increases, the strut effect gradually disappears, and the damage to the infilled wall is concentrated at the sliding layer or the connection between the sliding layer and the column, indicating that SBS sliding layers weaken the strut effect resulting in a significant reduction in the in-plane damage of infilled wall. Figure 18a shows a comparison of the load-displacement curves of the specimens with a different number of SBS layers. The specimens using one and two SBS layers presented a similar behavior until R = 1.5%, but the specimen with three layers possessed a much lower capacity than the others. From the point of view of reducing in-plane damage and improving in-plane bearing capacity for the infills, the preferred spacing of the SBS sliding layer in the infill wall is 1000 mm.

On the other hand, all specimens using steel plates possessed the same early linear behavior at the early stage until their ultimate loads, and then the lateral stiffness of the frames began to decrease. This is mainly due to the high coefficient of friction of the sliding layers. The increasing number of layers of steel plate did not lead to a decrease in the capacity of the frames, on the contrary, using more SBS layers can increase the slippage

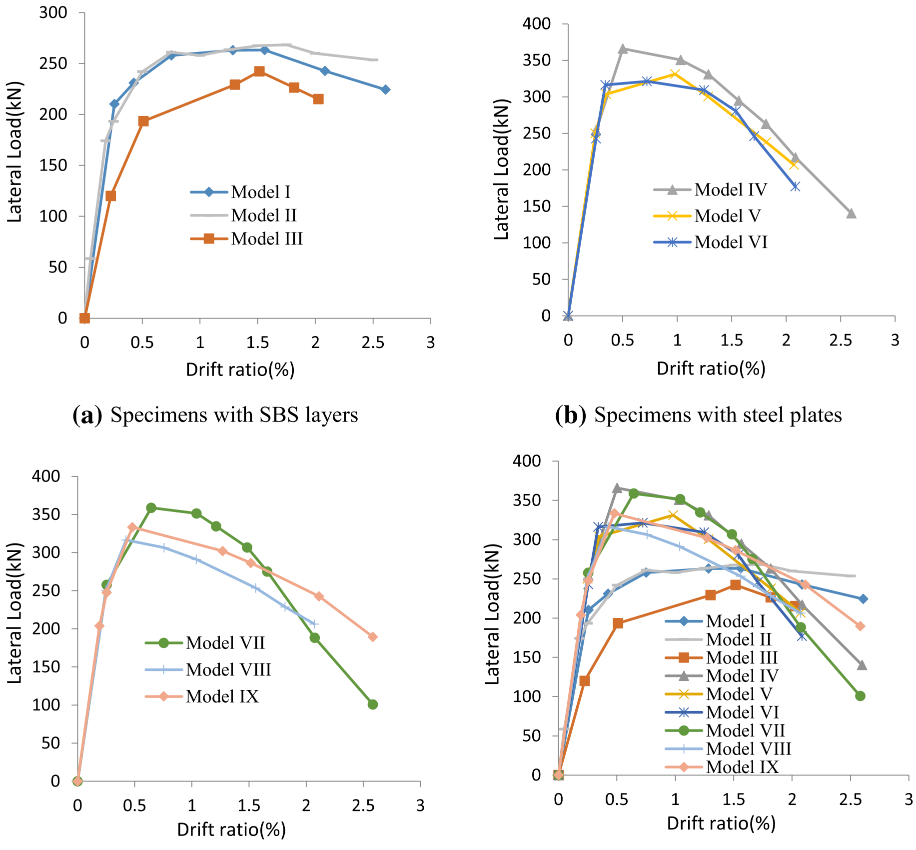

(a) Specimens with SBS layers **(b)** Specimens with steel plates

(c) Specimens with BFRP laminates **(d)** All specimens

Fig. 18 Effectof the spacing of layers in the frames between the layers and wall, which then resulted in a degradation in the peak loads. Therefore, as shown in Fig. 18b, the number of layers has a negative influence on the peak loads of the frames but made the frames present a similar post-peak behavior to the model specimens. A similar result was confirmed in the specimens with BFRP laminate (see Fig. 18c). Because the BFRP layers are non-ductility materials with a large slippage, the load-carrying capacity of the frames with BFRP laminate layers is reduced significantly. The stiffness of the frames significantly decreased after peak load, especially for the frames with fewer laminate layers. However, the stiffness of the BFRP specimens decreased with an increasing number of sliding layers, similar to the cases using steel plates, which also is similar to previous research (Mehrabi 1996; Al-Chaar 1998). Figure 18d presents the load-displacement behavior of all specimens, indicating that the load-carrying capacity of the frames with SBS layers is much smaller than that of the other frames.

(2) Effect of types of the materials of the layers

Figure 19a, b, and c show the load-displacement skeletoncurves of the specimens with the same layer spacing but different sliding layermaterials. When using the same layers of steel

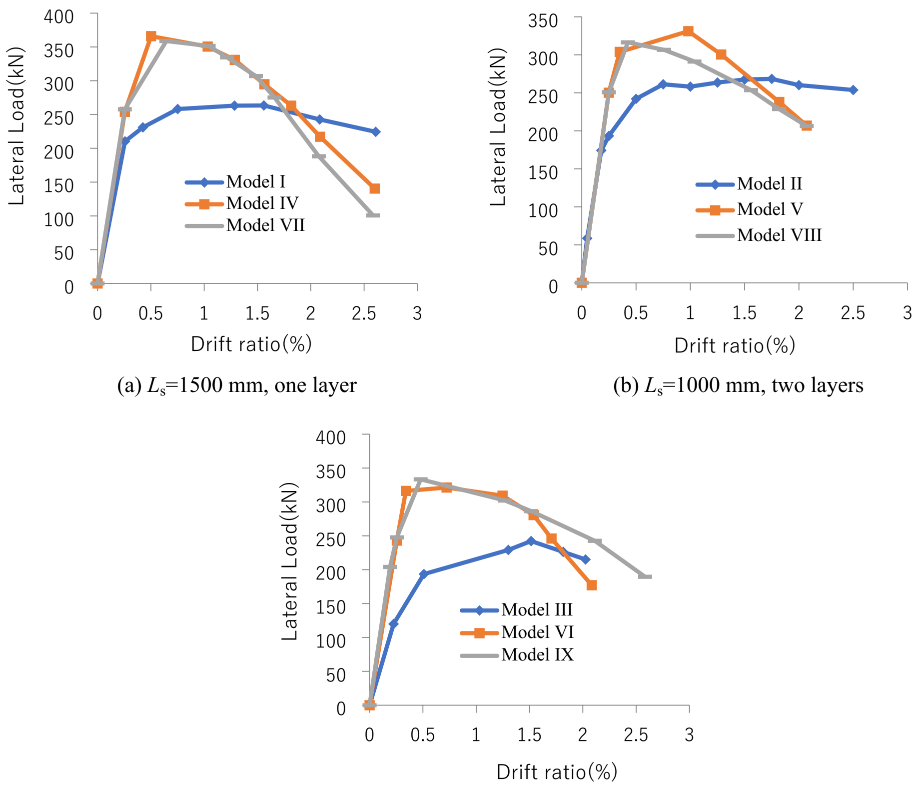

(a) L_s=1500 mm, one layer

(b) L_s=1000 mm, two layers

(c) L_s=750 mm, three layers

Fig. 19 Effect of the materials of sliding layers on infilled walls plate or BFRP laminate, the load-displacementbehavior of the frames was thesame, including initialelastic behavior, load-carrying capacity, and post-peak behavior. Due tothe coefficient of friction of SBS layers, the use of the layers significantly reduced theultimate load and accelerated the degradation of the load at post-peak. But thespecimens using SBS layers can still present similar initial stiffness to theother specimens.

5.3 Wall collapse ratios of infilled frames

The wall collapse ratio γproposed by the first and second authors (Cai and Cai 2017) was used in this section to evaluate the damage evolution quantitatively of the infilled walls in RC frames, which is given as:

$$\gamma = \frac{A_{cp}}{A_p} \times 100\% \tag{6}$$

where A_{cp} is the collapsed and crushed area of infilled walls, A_p is the total area of the infilled wall of RC frames. To understand the influence of different measures on the in-plane damage of infilled walls, Specimen R1(RC frame 0% in Cai and Cai 2017) and Specimen R2 (RC frame 25.7% in Cai and Cai 2017) are applied here for a comparative analysis of the collapse of the MHB-infilled RC frames. The dimensions of frame elements and infilled materials in Specimens R1 and R2 were the same as that of Specimen 1. The connecting rebar length of Specimens R1 and R2 was only 700mmm. Specimen R1 was a fully infilled frame (the opening ratio is 0%), and the opening ratio of Specimen R2 was 25.7%. The collapse ratio–drift ratio curves of the tested infills are shown in Fig. 20a. Specimen 3 presented the lowest collapse ratio as drift ratios, γ=6.63%, indicating it has the highest resistance to wall collapse in the frames. That can be attributed to two points: (1) the additional RC detailing columns improves the deformation capacity of the frame, and (2) the gaps relieved the compression of the wall in the corner from the frame columns on both sides. Specimen 1 showed the highest collapse ratio at R=4%, which was 88.64%. The main damage occurred in the wall corners,

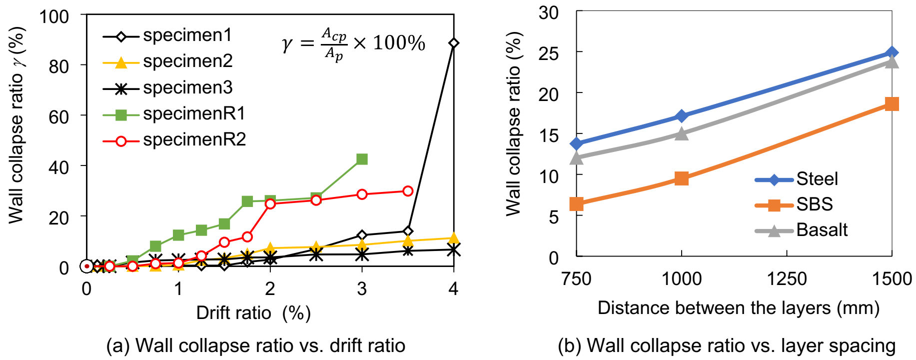

Fig. 20 Wall collapse ratios of the infilled RC frames

and the bricks were also severely crushed. The diagonal strut significantly improved the load-carrying capacity at the early stage, but the collapse ratio of the wall was also the highest, and almost all the bricks and mortar were crushed in the state of cyclic compression shearing. Besides, specimen 2 presented a small collapse ratio of the wall, which was 11.2% at R = 4%, in which the damage concentered only in the sliding layers. The value was higher than that of the specimen with gaps but much smaller than that of the specimen with the fully infilled wall. This is due to the sliding layers improving the restoring of the RC frame compared to the fully infilled frame, but the improvement was slightly less than that of the frame with gaps. It can be found that the longer connecting rebars can reduce the damage to the infilled wall by comparing Specimen R1 and Specimen 1, and the openings are also helpful in reducing the damage to the infilled wall (Specimen R2), as shown in Fig. 20a.

On the other hand, as shown in Fig. 20b, the collapse ratio of the infilled frames using SBS layers is much smaller than other specimens presenting similar wall collapse ratios. At the same time, the damaged area of the frames using more sliding layers was reduced significantly, regardless of the type of materials. The wall collapse ratios of the specimens decreased linearly with an increasing number of layers. Besides, it can be found that the longer connecting bars can reduce the damage to the infilled wall by comparing with the wall collapse ratio of Specimens R1 and 1 in Fig. 20. It is also suggested that the openings are conducive to reducing the damage to infilled walls.

5.4 Comparison of different control methods of infills in RC frames

Based on the above experimental and numerical results described above, main discussions on different control methods in MHB-infilled RC frames were summarized here, including the load-carrying capacity, energy dissipation, residual drift ratio, damage ratio, construction convenience, and ductility of the specimens, as shown in Fig. 21. For Specimen 1, the initial strong load-carrying capacity of the frame came from the strongest diagonal strut of the fully infilled wall. At the same time, fully infilling is also considered to be convenient for construction, compared to others. The main damages to the frame are the cracks in the frame and wall, wall collapse, brick compressive crushing, and the bending of connection rebars. However, the high residual deformation of the frame at the early stage hindered the resilience of the damaged infilled wall in the frame. The loss of the diagonal strut made the

Fig. 21 Comparison of three control methods of the walls in the frames

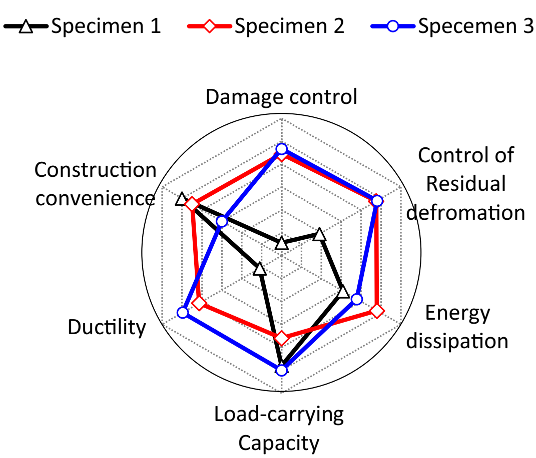

frame lower ductile than other frames due to sudden damage and collapse of the infill wall. Since the determination of the maximum load carrying capacity of this type of structure was controversial in previous studies (Cai and Su 2019), it was proposed that the traditional ductility calculation methods were not suitable for MHB infilled frame structures. The observation results show that the deformation performance of this type of structure after the collapse of the wall was close to that of the bare frame structure. When the SBS layers were used, the residual deformation, damage control, and energy dissipation capacity of the infilled frame were improved significantly, but the construction convenience was not improved much and the capacity and ductility of the frame were slightly reduced. Except for the construction convenience and energy dissipation capacity, the use of gaps and detailing columns improved the other performance of the infilled frames, such as Specimen 3 in Fig. 21.

6 Main conclusions

In this study, the seismic behavior of three one-bay one-story RC frames with masonry infilled walls with different damage control methods was experimentally and numerically investigated. The main conclusions are drawn here,

(1) The walls of the fully infilled RC frame eventually collapsed, while the frame columns and beams were severely damaged locally. Its failure mode was diagonal crushing and the final failure of the wall of the frame was greatly controlled after adding sliding layers and using gaps with detailing columns. Among them, the main failure of the frame with sliding layers was the diagonal crushing between the layers, while that of the frame with gaps was the diagonal bracing crushing after the gaps are closed due to the damage and deformation of the frame.
(2) The fully infilled frame exhibited larger load-carrying capacity and stiffness before wall collapse, and the highest energy dissipation capacity, but larger residual deformation. After the infilled wall collapsed, the frame behaved as a bare RC frame. The final residual deformation was relatively large due to the accumulation of the damages in the early stage.
(3) Due to the addition of the SBS sliding layer, the stiffness of the infill walls was reduced, resulting in the lateral stiffness and the peak load of the infilled frame being reduced.
(4) The utilization of gaps and detailing columns allowed the load-carrying capacity of the frame to be between the fully infilled frame and the frame with sliding layers, before the gaps were closed, after which the frame exhibited as a fully infilled frame. The frame presented an improved initial stiffness and energy dissipation capacity compared with the frame with sliding layers.
(5) The parametric analysis results showed that the main failure of the frames using sliding layers was SS failure mode, and the damage degree mainly depended on the number of sliding layers. With more sliding layers, the damage of the frames was better controlled, but their load-carrying capacity and energy dissipation were reduced. Regarding the effect of the material type of sliding layers, steel plate and SBS layers both exhibited similar damage control effectiveness. Based on the study, using SBS sliding layers with a spacing of 1000 mm was recommended to control the wall damage of the MHB-infilled frames.

Funding The authors thank the support from the science and technology fund of Chengdu fourth construction engineering of CDCEG, CCCC tunnel engineering company limited (2021 R110121H01083).

Declarations

Conflict of interest The authors declare that they have no known competing financial interests or personal relationships that could have appeared to influence the work reported in this paper.

References

Abaqus GUI (2011) Abaqus 6.11. Users Manual 6.11

Abdulla KF, Cunningham LS, M GIllie, (2017) Simulating masonry wall behaviour using a simplified micro-model approach. Eng Struct 151:349–365

Al-Chaar GK (1998) Non-ductile behavior of reinforced concrete frames with masonry infill panels subjected to in-plane loading. The University of Illinois, Chicago

Aliaari M, Memari AM (2005) Analysis of masonry infilled steel frames with seismic isolator subframes. Eng Struct 27(4):487–500

Bartolomeo Pantò I, Caliò, Paulo B, Lourenço (2017) Seismic safety evaluation of reinforced concrete masonry infilled frames using macro modelling approach. Bull Earthq Eng 15(9):3871–3895

Cai G, Su Q, Cai H (2017) Seismic behaviour of full-scale hollow bricks-infilled RC frames under cyclic loads. Bull Earthq Eng 15(7):2981–3012

Cai GC, Su QW (2019) Effect of infills on seismic performance of reinforced concrete frame structures—a full-scale experimental study. J Earthquake Eng 23(9):1531–1559

Campilho RD, De Moura M, Domingues J (2008) Using a cohesive damage model to predict the tensile behaviolur of CFRP single-straprepairs. Int J Solids Struct 45(5):497–512

Carreira DJ, Chu KH (1985) Stress-strain relationship for plain concrete in compression. J Am Concr Inst 82(6):797–804

Carreira DJ, Chu KH (1986) Stress-strain relationship for reinforced concrete in tension. J Am Concr Inst 83(1):121–28

Costa A, Miranda Guedes J, Varum H (2014) Structural rehabilitation of old buildings. Springer, Berlin, Heidelberg

Dhir PK, Tubaldi E, Ahmadi H (2021) Numerical modelling of reinforced concrete frames with masonry infills and rubber joints. Eng Struct 246:112833

Du Beton CE-I (1996) RC frames under earthquake loading: state of the art report. Telford, London

El-dakhakhni WW, Asce SM, Elgaaly M, Asce F, Hamid AA (2003) Three-strut model for concrete masonry-infilled steel frames. J Struct Eng 129(2):177–185

Erol G, Karadogan HF (2016) Seismic strengthening of infilled reinforced concrete frames by CFRP. Compos Part B Eng 91:473–491

Goncalves AMN, Guerreiro LMC, Candeias P, Ferreira JG, Campos Costa A (2018) Characterization of reinforced timber masonry walls in ‘Pombalino’ buildings with dynamic tests. Eng Struct 166:93–106

Hamid AA, El-dakhakhni WW, Asce M, Hakam ZHR, Elgaaly M, Asce F (2005) Behavior of composite unreinforced masonry—fiber-reinforced polymer wall assemblages under in-plane loading. J Compos Constr 9(1):73–83

Ivo C, Bartolomeo P (2014) A macro-element modelling approach of infilled frame structures. Comput Struct 143:91–107

Jacobsen LS (1960) Damping in composite structures. In: Proceedings of the 2nd world conference on earthquake engineering, 2, pp 1029–1044

Lee J, Fenves GL (1998) Plastic-damage model for cyclic loading of concrete structures. J Eng Mech 124(8):892–900

Lourenço PB (1996) Computational strategies for masonry structures, Thesis PhD 1996. www.civil.uminho.pt/masonry

Lubliner J, Oliver J, Oller S, Onate E (1989) A plastic-damage model for concrete. Int J Solids Struct 25(3):299–329

Mander JB, Aycardi LE, Kim DK (1994) Physical and analytical modeling of brick infilled steel frames. *Technical Report*, NCEER 94 – 0004, Buffalo

Mehrabi BA, Shing PB, Michael PS, James LN (1996) Experimental evaluation of masonry-infilled RC frames. J Struct Eng 122(3):228–237

Ministry of Housing and Urban-Rural Development of the PRC (2002) Standard for test method of mechanical properties on ordinary concrete (GB/T 50081 – 2002). China Building industry press, Beijing

Ministry of Housing and Urban-Rural Development of the PRC (2010) Code for design of concrete sructures (GB50010-2010). Standards press of China, Beijing

Ministry of Housing and urban-Rural Development of the PRC (2009) standard for test method of performance on building mortar(JGJ/T70-2009). China Building industry press, Beijing
Moghadam HA, Mohammadi M, Gh, Ghaemian M (2006) Experimental and analytical investigation into crack strength determination of infilled steel frames. Constr Steel Res 12(62):1341–1352
Pam H, Kwan A, Islam MS (2001) Flexural strength and ductility of reinforced normal-and high-strength concrete beams. Proc Inst Civil Eng Struct Build 146(4):381–389
Paulay T, Priestley MN (1992) Seismic design of reinforced concrete and masonry buildings. Wiley
Perera R, Gómez S, Alarcón E (2004) Experimental and analytical study of masonry infill reinforced concrete frames retrofitted with steel braces. J Struct Eng 130(32):2032–2039
Preti M, Bettini N, Migliorati L, Bolis V, Stavridis A, Plizzari GA (2016) Analysis of the in-plane response of earthen masonry infill panels partitioned by sliding joints. Earthq Eng Struct Dyn 45(8):1209–1232
Preti M, Neffati M, Bolis V (2018) Earthen masonry infill walls: use of wooden boards as sliding joints for seismic resistance. Constr Build Mater 184:100–110
Preti M, Bolis V, Stavridis A (2019) Seismic infill–frame interaction of masonry walls partitioned with horizontal sliding joints: analysis and simplified modeling. J Earthq Eng 23(10):1651–1677
Proença JM, Gago AS, Costa AV (2012) Strengthening of masonry wall load bearing structures with reinforced plastering mortar solution. *Proceedings of the 15th world conference on earthquake engineering* No. 2004, pp 1–10
Sahota MK, Riddington JR (2001) Experimental investigation into using lead to reduce vertical load transfer in infilled frames. Eng Struct 23(1):94–101
Sevil T, Baran M, Bilir T, Canbay E (2011) Use of steel fiber reinforced mortar for seismic strengthening. Constr Build Mater 25(2):892–899
Soti R, Barbosa AR, Stavridis A (2014) Numerical modeling of URM infill walls retrofitted with embedded reinforcing steel. *10th U.S. National Conference on Earthquake Engineering: Frontiers of Earthquake Engineering*, Anchorage, Alaska
State General Administration of the People's Republic of China for Quality Supervision and Inspection and Quarantine (2018) Steel for the reinforcedment of concrete—part 2: hot rolled ribbed bars (GB/T 1499.2–2018). Standards press of China, Beijing
Triantafillou TC (1998) Shear strengthening of reinforced concrete beams using epoxy-bonded FRP composites. ACI Struct J 95(2):107–115
Triwiyono A, Nugroho ASB, Firstyadi AD, Ottama F (2015) Flexural strength and ductility of concrete brick masonry wall strengthened using steel reinforcement. Proc Eng 12:940–947
Uva G, Raffaele D, Porco F, Fiore A (2012) On the role of equivalent strut models in the seismic assessment of infilled RC buildings. Eng Struct 42:83–94
Wang YY (2020) Abaqus analysis user's guide: element. China Machine Press, Beijing (**in Chinese**)
Wang FC, Kang TB, Yang YS, Lu S (2015) Seismic behaviour of the wall-frame structure infilled with rubber concrete brick. J Shengyang Jianzhu Univ 31(4):661–670 (**in Chinese**)
William KJ, Warnke EP (1974) Constitutive model for the triaxial behavior of concrete. *Proceedings of the International Association for Bridge and Structural engineering*, pp 1–30
Yaman TS, Canbay E (2014) Seismic strengthening of masonry infilled reinforced concrete frames with steel-fibre-reinforced mortar. ICE Proc Struct Build 167(1):3–14
Yang W, Ou J (2011) A method of improving global seismic capacity based on failure-controlled of infill walls for infilled structures. Build Struct 41(8):34–39 (**in Chinese**)
Yanhua Y, Weimin S et al (2004) Experimental study on seismic behaviors of hollow block wall filled with foaming concrete. Earthq Eng Eng Vib 24(5):154–158 (**in Chinese**)
Yun Z, Yangzhao G, Yifa L et al (2014) Experimental study on seismic behavior of damped masonry in-filled reinforced concrete frame structures with SBS layers. China Civil Eng J 47(9):21–28 (**in Chinese**)
Zhou Yun G, Yangzhao L, Yifa et al (2013) Experimental study on the performances of damped infill wall unit. China Civil Eng J 46(5):56–63 (**in Chinese**)